# Cause of the localized maximum of X-ray emission in the morning sector: A comparison with electron measurements

N. Østgaard,[1,2] J. Stadsnes,[1] J. Bjordal,[1] R. R. Vondrak,[3] S. A Cummer,[3,4]
D. L. Chenette,[5] M. Schulz,[5] and J. G. Pronko[6]

**Abstract.** The Polar Ionospheric X-ray Imaging Experiment (PIXIE) on board the Polar satellite has provided the first global scale views of the patterns of electron precipitation through imaging of the atmospheric X-ray bremsstrahlung. While other remote sensing techniques like UV and visible imaging sense emissions that are dominantly produced by low-energy electrons (<10 keV), the PIXIE X-ray images used in this study respond to electrons of energy above ~3 keV. From a statistical study of global X-ray emission a localized maximum in the morning sector, delayed with respect to substorm onset, is found to be a common feature during substorms. The time delay of this morning precipitation relative to substorm onset strongly indicates that this localized maximum is caused by electrons injected in the midnight sector drifting into a region in the dawnside magnetosphere where some mechanism effectively scatters the electrons into the loss cone. In this study we have examined two isolated substorms that occurred on July 31, 1997, and September 4, 1997, to investigate these features in more detail. PIXIE images are used to examine the global structures of the two events. Particle measurements from several low-altitude satellites, NOAA and DMSP, have provided fine structure information of the spatial and spectral development of the morning precipitation. We find good spatial correlation between X-ray emission and electron measurements for both these events. Comparison of measured electron spectra and electron spectra derived from X-ray measurements by PIXIE are also presented and correlates fairly well. The technique for deriving electron characteristics from the X-ray measurements are described and discussed. We find that both the electron spectra and the X-ray spectra can be represented by double or single exponentials. The electron spectra measured in the early stage of the localized morning maximum of X-ray emission strongly indicates that the scattering of >2-10 keV electrons by wave-particle interaction into the loss cone is the main mechanism for this precipitation.

## 1. Introduction

Until recently, global imaging of the energetic electron precipitation has not been available. Our knowledge of this part of the substorm has been based on measurements of cosmic radio noise absorption (riometer) [*Hartz and Brice*, 1967; *Jelly and Brice*, 1967; *Berkey et al.*, 1974], X-ray measurements from balloon campaigns [*Barcus and Rosenberg*, 1966; *Bjordal et al.*, 1971; *Sletten et al.*, 1971; *Kangas et al.*, 1975], particle measurements in space [*McDiarmid et al.*, 1975; *Hardy et al.*, 1985], and X-ray measurements from low-altitude satellites [*Imhof et al.*, 1980; *Chenette et al.*, 1992]. The Polar Ionospheric X-ray Imaging Experiment (PIXIE) on board the Polar satellite is the first true two-dimensional imaging instrument developed to measure the global X-ray emission simultaneously. As the X rays are produced by high-energy electrons interacting with the atmosphere, PIXIE provides the ability of studying both the spatial and temporal patterns of the global energetic electron precipitation during substorms.

From several statistical studies based on satellite measurements [*McDiarmid et al.*, 1975; *Hardy et al.*, 1985; *Codrescu et al.*, 1997], riometer measurements [*Hartz and Brice*, 1967; *Jelly and Brice*, 1967; *Berkey et al.*, 1974], and global images in UV [*Liou et al.*, 1997] and X rays [*Petrinec et al.*, 1998], there are found to exist two maximum regions of energetic precipitation but three maxima in the softer precipitation (<1 keV). *McDiarmid et al.* [1975] and *Hardy et al.* [1985] studied electron measurements in the energy range from tens of eV up to tens of keV, *Codrescu et al.* [1997] studied electrons from 30 keV to 2.5 MeV, while *Jelly and Brice* [1967] and *Berkey et al.* [1974] studied absorption of cosmic radio noise, which is sensitive to electrons of energies from 10 to 100 keV. Focusing on the energetic precipitation, all these studies found the first and most intense maximum to be situated around midnight and to be related to the injection of fresh electrons. They found another maximum to be located between dawn and noon, most probably related to the drifting electrons. However, by focusing on electron precipitation at lower energies (<1 keV), there is found to exist an additional maximum in the postnoon region [*McDiarmid et al.*, 1975; *Liou et al.*, 1997] where an almost complete lack of X-ray emission is observed [*Petrinec et al.*, 1998]. All of these studies, except for the study of *Berkey et al.* [1974], were based on adding all the observed precipitation during all kinds of geomagnetic activity and provide no information on the temporal behavior of single substorms. However, a statistical study of 14 isolated substorms during 1996 [*Østgaard et al.*, 1999b] using PIXIE and UVI data from the Polar

[1]Department of Physics, University of Bergen, Bergen, Norway.
[2]Now at Department of Physics, University of Oslo, Oslo, Norway.
[3]Laboratory for Extraterrestrial Physics, Goddard Space Flight Center, Greenbelt, Maryland.
[4]Now at Department of Electrical and Computer Engineering, Duke University, Durham, North Carolina.
[5]Lockheed Martin Advanced Technology Center, Palo Alto, California.
[6]Physics Department, University of Nevada, Reno.

satellite combined with ground-based measurements and data from geosynchronous satellites have confirmed many of these global characteristics.

In this paper we examine two isolated substorms, occurring on July 31, 1997, and September 4, 1997, to further investigate the localized morning maximum of X-ray emission, how it is related to the substorm onset, and the mechanism that causes this maximum. The global PIXIE images are used to infer the large-scale dynamics of the substorms and the electron measurements from National Oceanic and Atmospheric Administration spacecraft 12 (NOAA 12) and the Defense Meteorological Satellite Program spacecraft F12, F13, and F14 (DMSP F12, F13, and F14), all in polar orbits of ~800 km altitude, are used to examine the fine structures in the same region. The combined measurements of X rays and electrons are used (1) to correlate the directly measured X-ray profiles and the derived X-ray profiles from the electron measurements, (2) to compare the directly measured electron spectra and the derived electron spectra from the X-ray measurements and, (3) based on the electron spectral information in the region of localized morning precipitation we suggest the most probable mechanism that causes the observed localized maximum of X-ray emission.

## 2. Instrumentation

The PIXIE camera provides images of the X-ray bremsstrahlung seen during substorms. Even though the probability of generating an X-ray photon from an electron slowing down in the atmosphere increases as a function of the initial electron energy, for a 200 keV electron the probabilty of producing an X-ray photon at an energy below 200 keV is only 0.5% [*Berger and Seltzer*, 1972]. Nevertheless, these measurements provide the opportunity to study the global energetic electron precipitation, even in the sunlit area. The instrument is a pinhole camera with four stacked multiwire proportional counters as detecting elements. Two detectors are in the front chamber, which contains a 1.1-atm $Ar/CO_2$ mixture, has a 0.1-mm Be entrance window, and is sensitive to X-ray photons from ~2 to ~10 keV. The rear chamber, with a 2-atm $Xe/CO_2$ mixture and a 2-mm Be window, contains the other two detectors and covers the energy range from ~10 to ~60 keV [*Imhof et al.*, 1995]. A background subtraction scheme has been provided by accumulating hours of data when no aurora or celestial sources were seen, giving an average background due to particles, cosmic X rays and X rays produced in the surrounding structures of the instrument by energetic particles. This average background, obtained separately for each energy band, is subtracted to obtain images of the genuine auroral X rays in different energy bands.

Owing to a problem with the high-voltage supply in the front chamber of the PIXIE instrument, which measures the low-energy X rays, the front chamber had to be duty cycled with 5 min on and 10 min off for most of 1997. However, the rear chamber measuring the high-energy X rays provides continuous measurements. Restricted by this duty cycling of the front chamber 4.5-min accumulation has been used for the images in the low-energy range and 10-min accumulation has been used for the images in the upper energy range in order to get sufficient count rates to make images. The larger accumulation time for the upper energy range is centered around the center time for the 4.5 min accumulation time in the lower-energy range in order to make the images comparable. For the comparison with electron measurements from the NOAA 12 and DMSP satellites the accumulation time interval for the high-energy X rays is chosen in order to correspond with these measurements. For all the data used in this paper the X-ray production layer is assumed to be at 100-km altitude.

At the NOAA 12 spacecraft we use the data from the Total Energy Detector (TED) and the Medium Energy Proton and Electron Detector (MEPED) [*Raben et al.*, 1995]. The NOAA 12 satellite is in a Sun-synchronous, low-altitude polar orbit. The orbital period is 101 min and the altitude is 824 km at apogee and 804 km at perigee. TED is an electrostatic analyzer, MEPED is a solid-state detector, and they are covering different energy ranges and pitch angles. TED has 11 energy channels from 300 eV to 20 keV looking at 0˚ and 30˚ local zenith angles. Only 4 channels and the total energy flux (based on all 11 channels) are telemetered. MEPED has two sensors looking at 10˚ and 80˚ local zenith angles measuring integral count >30, >100, and >300 keV. Assuming that the main energy deposition is occurring at ~100 km altitude, the loss cone at 850 km is found to be within ~50˚ pitch angle in the Northern Hemisphere above 50˚ magnetic latitude. As the two look directions of MEPED correspond to 0˚-25˚ and 65˚-95˚ pitch angle intervals, we obtain some information about the angular distribution and the boundary of isotropic precipitation. The look direction of the TED detector is always well within the loss cone above 50˚ magnetic latitude. Combining the measurements from both TED and MEPED, we obtain an electron spectrum every 2 s. In comparison with PIXIE measurements we have used 20-s-averaged spectra from NOAA 12 in order to improve the statistics.

The SSJ/4 electrostatic analysers on board the DMSP satellites measures electrons and ions from 32 eV to 30 keV in 19 logarithmically spaced steps [*Hardy et al.*, 1984]. The DMSP satellites are in a Sun-synchronous, low-altitude polar orbit. The orbital period is 101 min, and the nominal altitude is 830 km. One complete electron and ion spectrum is obtained every second. The satellites are three-axis stabilized, and the detector always points toward local zenith. At the latitudes of interest in this paper, this means that only particles at pitch angles <15˚, well within the atmospheric loss cone, are observed. In comparison with PIXIE measurements we have used 20-s-averaged spectra from the SSJ/4 at the DMSP spacecrafts.

## 3. Observations

### 3.1. Geomagnetic Conditions

In Figure 1 the geomagnetic conditions for the two events are shown. Figures 1a and 1b show the global *Dst* index and *Kp* index. Figures 1c and 1d show the provisional *AE* index from Kyoto. From the *Dst* index prior to the substorm on July 31 we notify a long period of rather quiet magnetic conditions. During the onset of the substorm the *Dst* index shows an abrupt decrease but only reaches about -20 and can hardly be called a magnetic storm although the shape of the *Dst* index shows a typical storm signature. On the other hand, the *Kp* is 4, and the *AE* index shows a very abrupt increase. The very large *AE* index (> 1000 nT) indicates a rather intense substorm. The other event on September 4, 1997, occurs in the recovery phase of a magnetic storm, the *Kp* index is only 2 and the *AE* index, which is based on all the eight stations increases to above 650 nT. Although the two substorms occur during different overall magnetic conditions, both substorms are isolated and have only one onset.

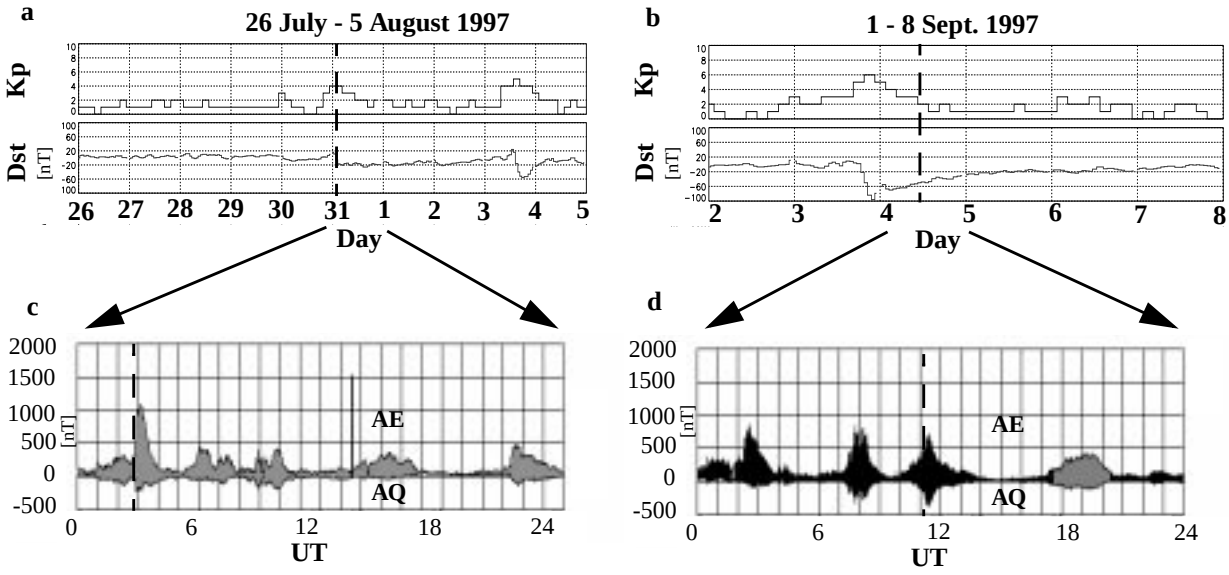


**Figure 1.** Magnetic conditions for the July 31 and September 4, 1997, events. (a, b) *Dst* and *Kp* index. (c, d) Provisional *AE* index from Kyoto, for the July 31 event based on four stations and for the September 4 event based on all the eight stations. The dashed lines indicate the onset time of the substorms. (Figure 1b and 1d are similar as Figure 1 of *Østgaard et al.* [1999a].)

### 3.2. X-ray Observations

In Plate 1 the two X-ray substorms are shown in two different energy ranges for each event, i.e., 2.8-9.9 keV and 7.9-21.3 keV for July 31 and 2.7-9.4 keV and 7.8-21.2 keV for September 4. The grid is corrected geomagnetic coordinates (CGM). In the first images from the low-energy range the celestial source Circinus X-1 is seen, entering at slant angle through adjacent pinholes of the PIXIE camera. Circinus X-1 is moving across the image as the Polar satellite proceeds in its orbit. As the energy spectrum of this neutron-star binary X-ray source is rather soft, it is not detectable in the higher-energy range of X rays. In Plate 1b the substorm onset (July 31 at 2000-2100 magnetic local time (MLT) and September 4 at 2100-2200 MLT, the determination of onset time and location is described below) is seen in both the energy ranges for both of the events followed by the eastward expansion (Plate 1c and 1d). The localized morning maximum of X-ray emission appears around 0600-0900 MLT in both the events. It should be noticed that the July 31 event is more intense than the September 4 event, which is consistent with the different values of the *AE* index for the two events. For the July 31 event the localized morning maximum is most clearly seen in the high-energy range and extends toward noon (Plate 1d and 1e). For the September 4 event the localized maximum is seen in both energy ranges but does not expand as much as for the July 31 event. A small intensification caused by a new injection is seen at 2100 MLT, September 4, in Plate 1e.

Using a similar method as described in *Østgaard et al.* [1999b] we have provided a time analysis of the X-ray emission along the auroral zone. Sectors of 2 hour MLT and 60° to 74° CGM latitude were used for both events to calculate the 5-min average flux within the area every 30 s. Such an analysis show that the substorm onsets occurred at 0240:30 UT in the 2000-2100 MLT sector, July 31 and at 1108:30 UT in the 2100-2200 MLT sector, September 4. The time analysis show that there is a rapid expansion of the injection front into the adjacent MLT sectors both westward and eastward for both the events, and during the recovery phase the X-ray features expand into the morning sector. The onset of the localized maximum were determined from the 0400-0600 MLT sector at 0254 UT, July 31 (13.5 min delayed relative to substorm onset) and from the 0500-0700 MLT sector at 1118:30 UT, September 4 (10.5 min delayed relative to substorm onset). In a previous work [*Østgaard et al.*, 1999a] these delay times were found to be in the same range as the delay times found in six other isolated substorms from 1996. By using a simple drift model by *Lew* [1961], which gave about the same values as a more realistic model developed by *Roederer* [1970] it was found that these delay times of X-ray features along the auroral zone correspond to precipitation from drifting electrons in the energy range of 90-170 keV [see *Østgaard et al.*, 1999a, Figure 5]. These findings confirm the results from others who have found drifting electron energies of ~140 keV [*Sletten et al.*, 1971], 100-200 keV [*Kangas et al.*, 1975] and 100 keV [*Berkey et al.*, 1974].

### 3.3. Electron Measurements and Functional Fits

In order to calculate the X-ray production from electron spectra we have to perform a functional fit to the electron measurements. From previous studies of X-ray measurements it has been found that a sum of two exponentials

$$\varphi(E) = \varphi_{01} e^{-E/E_{01}} + \varphi_{02} e^{-E/E_{02}}, \quad (1)$$

where $\varphi_{01}$ and $\varphi_{02}$ are the X-ray flux at zero energy and $E_{01}$ and $E_{02}$ are the two characteristic energies, very often can be used to represent the X-ray flux energy spectra, $\varphi(E)$ [e.g., *Goldberg et al.*, 1982]. From a rocket experiment in the postmidnight sector during the recovery phase of a substorm [*Østgaard et al.*, 1998] when both X-ray measurements and electron measurements were available it was found that both the electron spectrum and the X-ray spectrum could be represented by a sum of two exponentials, giving very good correlation when comparing measured and cal-

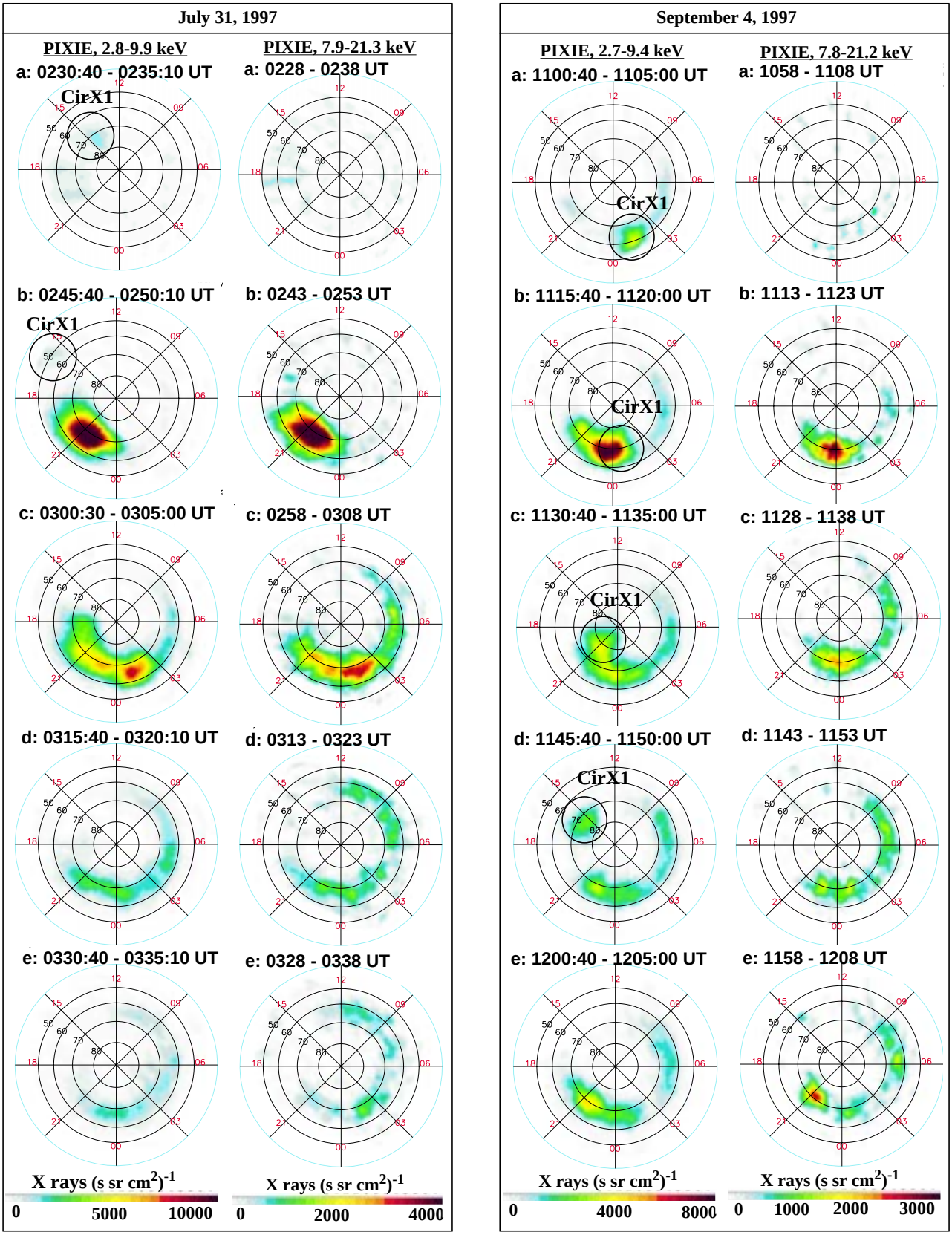


**Plate 1.** (left) July 31, 1997, integral X-ray flux in the energy range from 2.8 to 9.9 keV, 5-min accumulation. The celestial source Circinus X-1 is encircled. (middle left) July 31, 1997, integral X-ray flux in the energy range from 7.9 to 21.3 keV, 10-min accumulation. (middle right) September 4, 1997, integral X-ray flux in the energy range from 2.7 to 9.4 keV, 5-min accumulation.The celestial source Circinus X-1 is encircled. (right) September 4, 1997, integral X-ray flux in the energy range from 7.8 to 21.2 keV, 10-min accumulation. Corrected geomagnetic (CGM) grid is used.

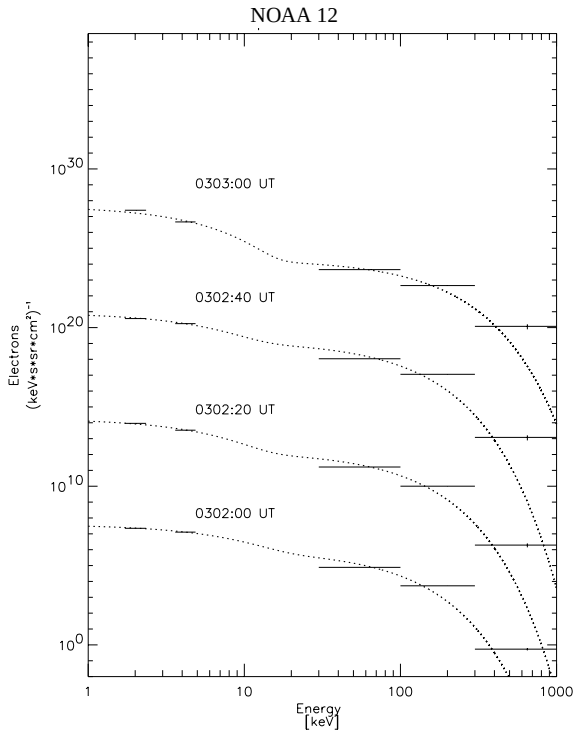


**Figure 2.** Electron spectra measured by NOAA 12, July 31, from 0302 to 0304 UT in the morning sector. Horizontal lines show the measurements and dotted lines show the double exponential fit to the measurements. Only measurements above 1 keV is used in the fit procedure.The spectra are shifted subsequently by 7 orders of magnitude.

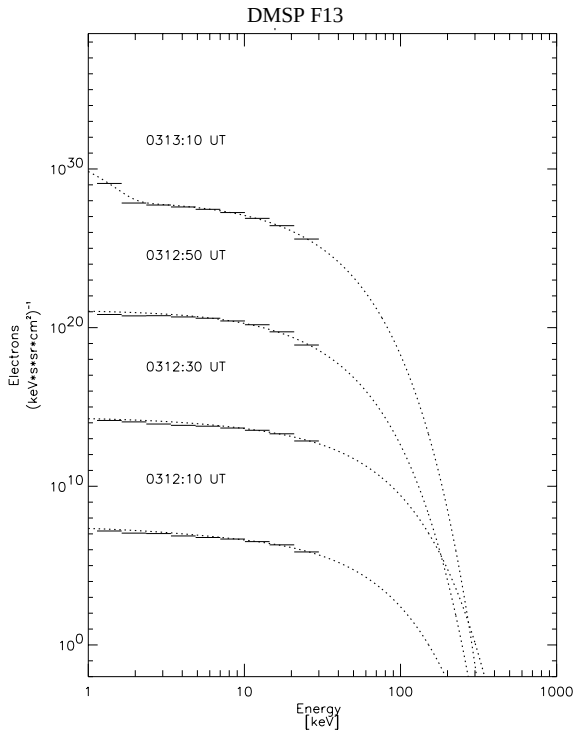


**Figure 3.** Electron spectra measured by DMSP F13, July 31, from 0312 to 0313 UT in the midnight sector. Horizontal lines show the measurements, and dotted lines show the double exponential fit to the measurements. Only measurements above 1 keV is used in the fit procedure. The spectra are shifted subsequently by 7 orders of magnitude.

culated electron spectra and measured and calculated X-ray spectra. To examine how good this functional fit works for the actual electron measurements, we show four spectra measured by NOAA 12 from a pass in the morning sector (Figure 2) and four spectra measured by DMSP F13 from a pass in the midnight sector (Figure 3). The 20-s averages has been used to obtain the electron spectra. From NOAA 12 we use the measurements from TED (four channels in the low-energy range) and convert the three high-energy integral channels from MEPED to differential flux, assuming the upper limit of the upper integral channel to be ~1000 keV. For the functional fit, only measurements above 1 keV are used, as electrons below ~3 keV are not able to produce the observed X rays. From Figure 2 it can be seen that the double exponential makes a good representation for all energies except for the uppermost channel. To represent the hard tail of this morningside spectrum, a Kappa function would probably have been more suitable, as proposed by others [e.g., *Sharber et al.*, 1998], but as our X-ray calculation procedure only allows exponentials and Maxwellians, we use the double exponential fits keeping in mind that the electron fluxes may be slightly underestimated for the high energies. From the DMSP satellites we obtain electron spectra from 19 channels from 0.3 to 30 keV. The double exponentials represent the measurements very well, but we do not know how good the fit is for energies above 30 keV. However, for these spectra at midnight the flux falls off rapidly in the upper channels, and we do not think there is any significant high-energy component for the spectra shown in Figure 3. An additional check (not shown) was made by comparing directly measured electron fluxes from 0.3 keV to 20 keV with electron fluxes based on the double or single exponential fits in the same energy range. The comparison showed very good correlation. On the basis of the Figures 2 and 3 we conclude that the double exponential fit can be used to represent the electron measurements from NOAA 12 and the DMSP satellites in the present study.

### 3.4. Comparison of Measured and Calculated X-ray Profiles

The double exponential fit to the electron spectra enables us to calculate the X-ray production along the magnetic footprints of the trajectories of NOAA 12 and DMSP satellite passes (Figures 4-6). The NOAA 12 passes (Figures 4b-d and Figures 6b-d) are from passes in the Northern Hemisphere, while the DMSP passes (spacecraft F13 and F14) are from the Southern Hemisphere. To compare the calculated X-ray fluxes from the electron measurements from the DMSP satellite passes with the directly measured X rays by PIXIE at the Northern Hemisphere we have traced the satellite trajectories along the magnetic field line (using CGM coordinates) into the Northern hemisphere giving the conjugate magnetic trajectories. The measured X rays along the magnetic footprint of the satellite are averaged within a circle with a diameter of ~500 km, and the spatial resolution of the PIXIE images from these apogee passes is 1000 km. However, as long as the averaging area is significantly smaller than the spatial resolution of the pinhole camera itself, the resulting spatial resolution of the X-ray profiles is basically determined by the spatial resolution of the camera, i.e., 1000 km.

A look-up table assuming isotropic electron precipitation gives us the X-ray production emitted at different zenith angles as a

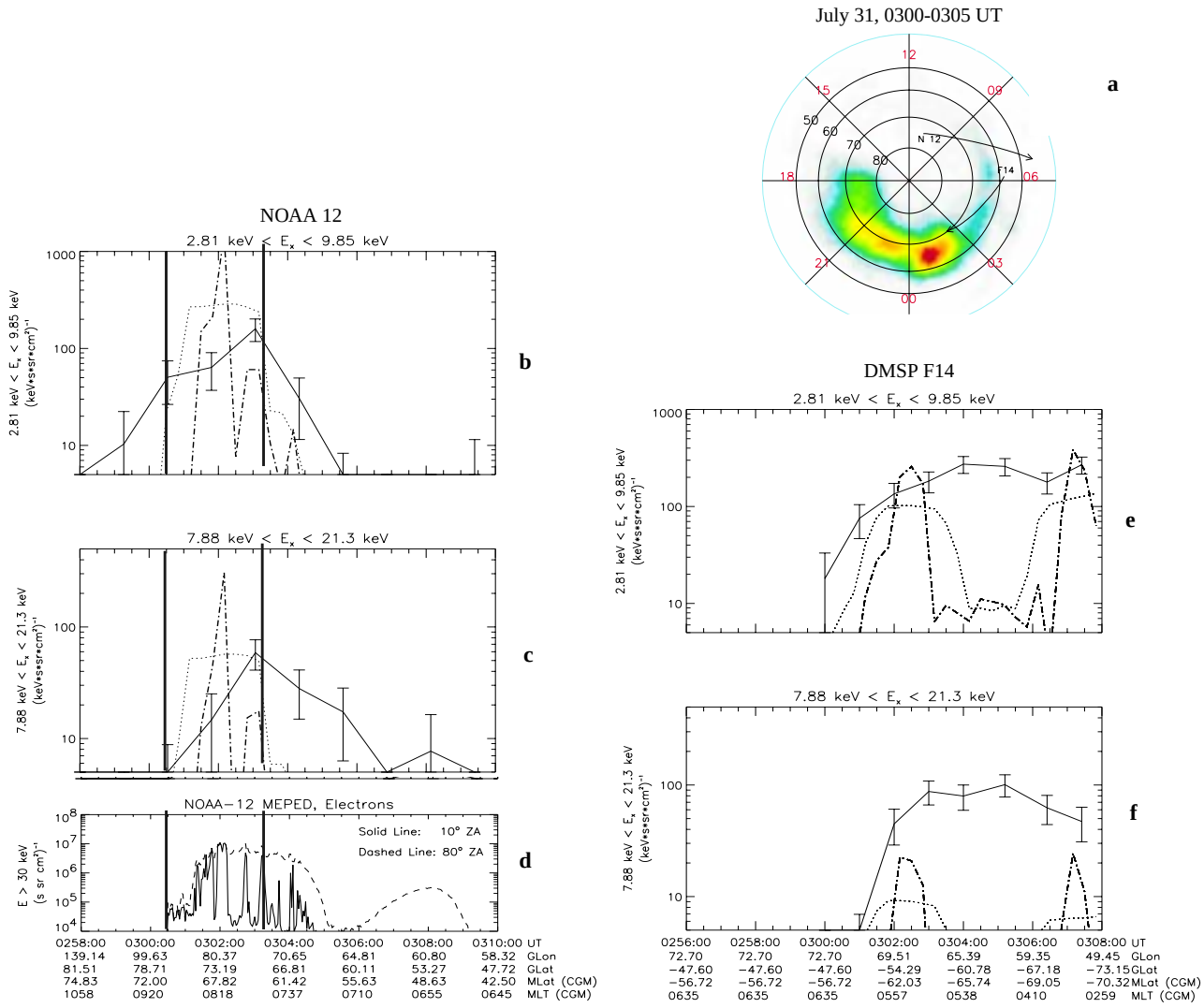


**Figure 4.** Measured and calculated X rays along the magnetic footprints of three satellite passes, July 31. (a) The trajectories of NOAA 12 (0258-0310 UT) and DMSP F14 (0256-0308 UT, conjugate magnetic position) (b, e) Measured and calculated X rays 2.8-9.9 keV. Solid lines show the measured X-ray fluxes accumulated from 0300 to 0305 UT. Dashed-dotted lines (dotted lines) show the unsmoothed (smoothed) calculated X-ray production from the electron spectra measured by TED and MEPED (NOAA 12) and by the SSJ/4 particle detector (DMSP). (c, f) Solid lines show the measured X rays from 7.9-21.3 keV, accumulated from 0300 to 0305 UT. Dashed-dotted lines (dotted lines) show the unsmoothed (smoothed) calculated X-ray production from the measured electron spectra. (d) The integrated electron flux >30 keV measured by MEPED (NOAA 12, 0258-0310 UT). Solid line are the electron flux at 10˚ local zenith and dashed line at 80˚ local zenith. Vertical lines indicate the partly isotropic flux region.

function of single exponentials. This look-up table is provided by a coupled electron photon transport code originally derived from neutron transport codes [*Lorence*, 1992]. In this case the transport is of electrons and photons and includes bremsstrahlung production, Compton scattering, photoabsorption, and radiation by secondary electrons. By adding the X-ray outcome from the two exponentials and integrating the X-ray fluxes in the energy ranges 2.8-9.9 keV and 7.9-21.3 keV for the July 31 event and 2.7-9.4 keV and 7.8-21.2 keV for the September 4 event we get the calculated X rays from each electron spectrum, shown by dashed-dotted lines in Figures 4-6. It should be noticed that the electron spectra from NOAA 12 are based on the electron measurements at pitch angles less than 25˚ and the electron measurements from DMSP satellites are at pitch angles <15˚. At 800 km altitude we estimated the loss cone to be within a pitch angle of ~50˚, which means that the spectra from both NOAA 12 and the DMSP satellites only provide information of the total electron precipitation in the region of isotropic electron fluxes. The profiles of the calculated X-ray production are smoothed by a running average of 140 s (i.e., over 1000 km along the satellite orbit) in order to be comparable to the spatial resolution of the measured X-ray profiles (i.e., 1000 km). The smoothed calculated X rays from the electron measurements are shown by dotted lines and the directly measured X-ray profiles are shown by solid lines in all the plots.

Figure 4 shows the measured and calculated X-ray profiles for July 31 through the region of maximum X-ray emission in the morning sector. For this event we found the onset of the localized maximum in the morning sector to occur at 0254 UT in the 0400-0700 MLT sectors and the satellite measurements by both NOAA 12 and DMSP F14 are taken from just this time interval (0258-0310 UT and 0256-0308 UT). The satellite trajectories are shown in Figure 4a. From the electron measurements by MEPED on

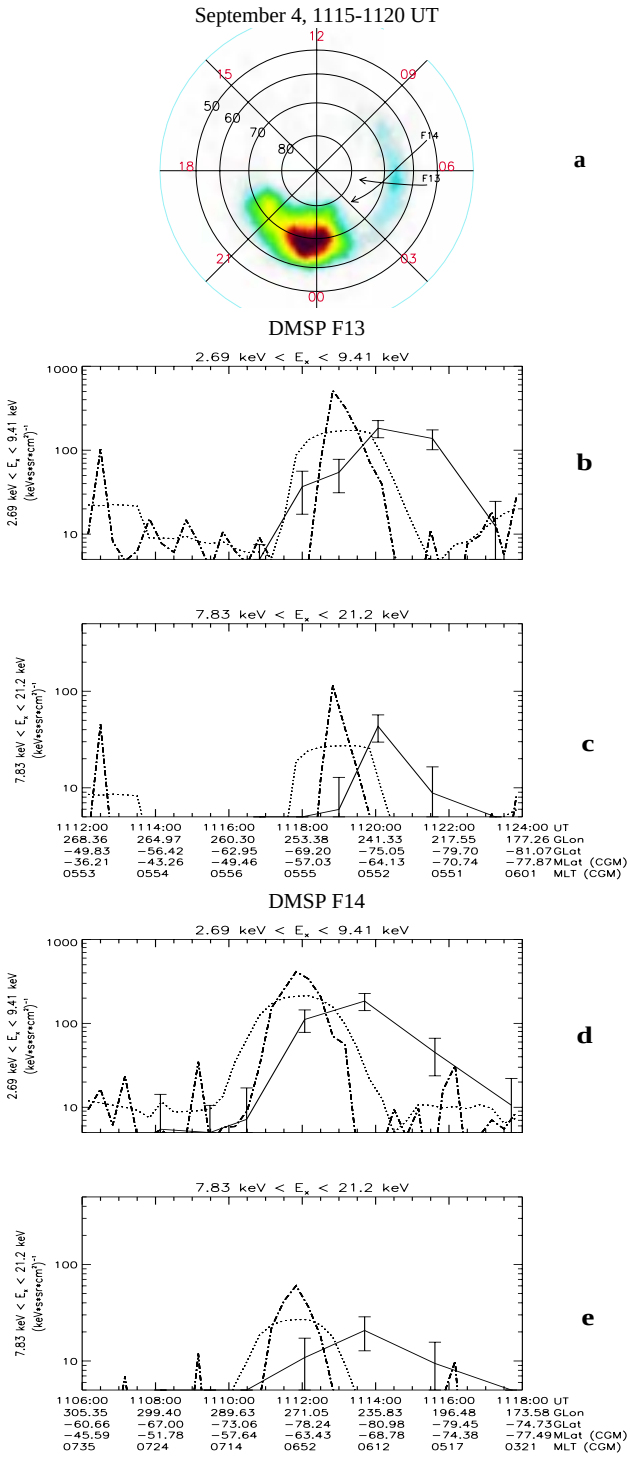


**Figure 5.** Measured and calculated X rays along the conjugate magnetic footprints of 2 DMSP satellite passes, September 4. (a) The trajectories of DMSP F13 (1112-1124 UT) and F14 (1106-1118 UT). (b, d) Solid lines show the measured X rays, 2.8-9.9 keV, accumulated from 1115 to 1120 UT. Dashed-dotted lines (dotted lines) show the unsmoothed (smoothed) calculated X-ray production (2.8-9.9 keV) from the measured electron spectra. (c, e) X rays in the energy range from 7.9 to 21.3 keV. Solid lines show the measured X rays, accumulated from 1115 to 1120 UT (Figure 5b) and from 1108 to 1116 UT (Figure 5d). Dashed-dotted lines (dotted lines) show the unsmoothed (smoothed) calculated X-ray production from the measured electron spectra (7.9-21.3 keV).

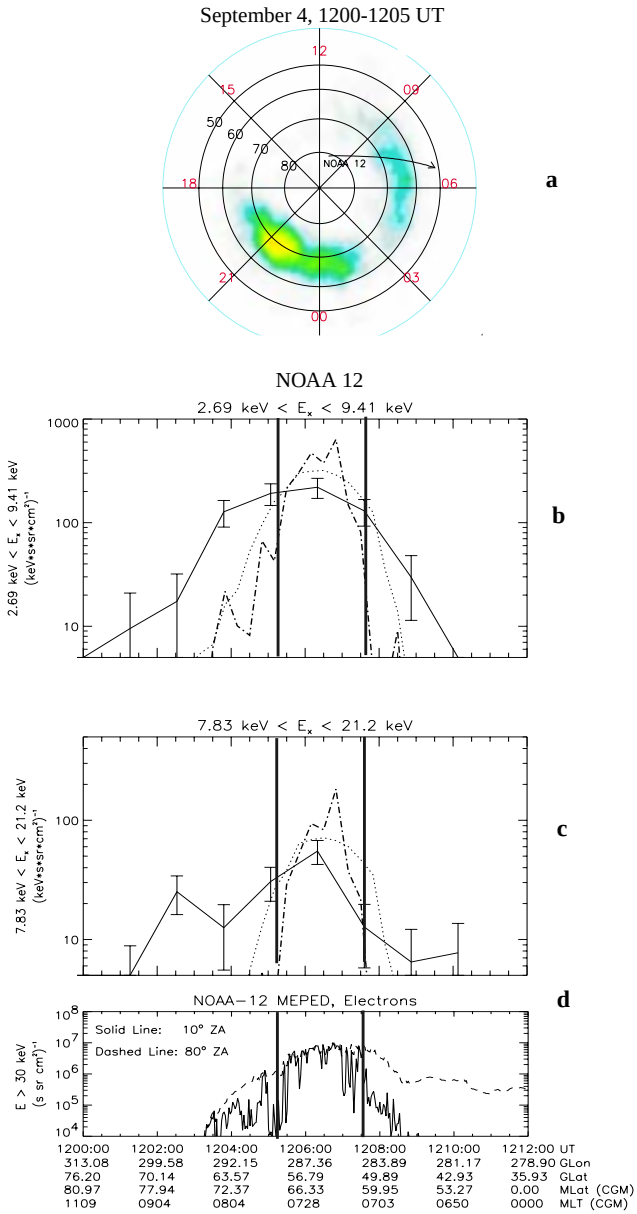


**Figure 6.** (a) The trajectories of NOAA 12 (1200-1212 UT). (b) Solid line shows the measured X-ray fluxes, 2.7-9.4 keV, accumulated from 1200 to 1205 UT. Dashed-dotted lines (dotted lines) show the unsmoothed (smoothed) calculated X-ray production from the electron spectra measured by TED and MEPED (NOAA 12). (c) Solid lines show the measured X rays from 7.9-21.3 keV, accumulated from 1202 to 1210 UT. Dashed dotted lines (dotted lines) show the unsmoothed (smoothed) calculated X-ray production from the measured electron spectra. (d) The integrated electron flux >30 keV measured by MEPED (NOAA 12). Solid line are the electron flux at 10˚ local zenith and dashed line at 80˚ local zenith. Vertical lines indicate the partly isotropic flux region. (Same as Figure 6d and Figure 8 of *Østgaard et al.* [1999a])

board NOAA 12 (Figure 4d) we obtain information about the pitch angle distribution, as the detectors measure at 10˚ local zenith angle and 80˚ local zenith angle (i.e., 0˚-25˚ and 65˚-95˚ pitch angle intervals at these magnetic latitudes). We have indicated the region of partly isotropic electron fluxes, even if the electron fluxes are rather structured with significant anisotropic

fluxes inside this region. In Figures 4b and 4c it can be seen that the calculated X rays correlate fairly well with the directly measured X rays in the isotropic region, while the measured X rays outside this region is probably caused by larger electron fluxes at pitch angles >25˚ (but within the loss cone) as the electron fluxes are anisotropic in this region. In the low-energy range of X rays (Figure 4b) the measured electron spectra tend to produce more X rays than the directly measured X rays indicate. This discrepancy is probably caused by locally structured electron precipitation. Such structures would be smoothed by the PIXIE field of view (FOV), but not by the point measurements of particles. We should emphasize that the smoothing of electrons can only be applied along the satellites trajectory and that any structures in the vicinity of this trajectory will not be detected by the satellites but will be within the region used to plot the X-ray profiles. Although the PIXIE accumulation time corresponds fairly well to the times of the NOAA 12 and DMSP F14 passes through the region of X-ray emission we can not disregard temporal variations in the electron precipitation seen by PIXIE but not by the two satellites. This must be kept in mind for all the comparisons between the insitu electron measurements and the accumulated PIXIE measurements.

The calculated X rays from the electron measurements by DMSP F14 are shown in Figures 4e-f. In the low-energy range of X rays the profiles correlate fairly well at the peaks of the measured electrons but deviate about an order of magnitude in the region between the peaks. As we do not have any pitch angle information from the DMSP measurements, it is most likely that the peaks seen in the calculated X-ray profiles are from the region of partly isotropic electron fluxes and the discrepancy in the region between the peaks are produced by anisotropic electron fluxes not seen by DMSP. The high-energy range of X rays (Figure 4f) shows a similar profile but is underestimated even in what we think is the isotropic region. This discrepancy is probably due to the lack of electron measurements at >30 keV and is discussed in the next section.

In Figure 5 the passes by DMSP F13 and F14 in the Southern Hemisphere through the region of localized maximum of X-ray emission are shown for the September 4 event. We found the onset of the electron precipitation in the morning sector to occur at 1118:30 UT in the 0500-0800 MLT sectors (using the method described by *Østgaard et al.* [1999b]) which means that the two DMSP passes are taken prior to (F14: 1111 UT) and at the onset of the localized morning precipitation (F13: 1118 UT). The correlation in both energy ranges are very good regarding the magnitude of measured and calculated X-ray fluxes, but there is a discrepancy in the location of the precipitation area measured in the two hemispheres probably due to uncertainties in the field line tracing between the hemispheres.

In Figure 6 we show a pass by NOAA 12 in Northern Hemisphere through the region of the morning maximum of X-ray emission September 4. The satellite passes the region ~45 min after the onset of the precipitation, but from the PIXIE image (Figure 6a) the prolonged enhancement is still observed. From Figure 6d it can be seen that the isotropic region of electron precipitation is larger and more homogenous than was the case for the July 31 event (Figure 4d). The measured and calculated X-ray profile correlate very well both in location and magnitude for both the energy ranges of X rays. The discrepancies outside the isotropic precipitation region are most probably due to electron fluxes within the loss cone at pitch angles >25˚.

### 3.5. Comparison of Measured and Derived Electron Spectra

Although the X-ray production increases with increasing electron energies the probability of X-ray production is still very small and X-ray measurements often suffer from poor statistics when spectral information shall be extracted. On the other hand, if it is possible to derive the electron spectra from the X-ray measurements a very strong tool is available to study the global energy deposition from global X-ray imaging. In this section we examine the electron spectra derived from the PIXIE X-ray measurements and compare with the directly measured electrons within the same area where the X-ray measurements are obtained.To obtain sufficient count rates we have binned the 63 energy channels of the low-energy section of PIXIE into four energy bands and the high-energy section of the detector into two energy bands. In Table 1 the time-dependent energy ranges of the different channels are listed, and it should be noticed that the upper channel of the front section overlap the lower channel of the rear section during both these events. Above channel 21 in the high-energy section of PIXIE the auroral X rays are contaminated by the fluorescence peak of Xenon and background noise and are therefore not used. To further improve the statistics, we have chosen areas of no less than 6˚ magnetic latitude and 1 hour MLT sector to obtain the area averaged fluxes in the six energy bands. In order to derive a double or single exponential electron spectrum from the X-ray spectrum we proceed as follows. By searching through the look-up tables of produced X-ray spectra from single electron spectra generated on the basis of the general electron-photon transport code of *Lorence* [1992], we find both a single exponential and four different double exponential electron spectra that may produce the measured X-ray spectra. In this procedure we superimpose the X-ray production from two single exponential electron spectra to obtain the X-ray spectra from double exponential electron spectra and interpolate between the values in the look-up table. By minimizing the Chisquares the single or double electron spectrum that may reproduce the observed X-ray spectrum is found. When more than one electron spectrum passes the Chi-square test, we choose the derived electron spectrum that gives the smallest electron energy flux, giving a lower limit of electron energy flux deposited in the ionosphere based on X-ray measurements. In Figures 7-10 we show the results of the derived electron spectra (from X-ray spectra) compared with directly measured electron spectra by NOAA 12 and DMSP satellites. It should be notified that for all the X-ray spectra shown here, channel 5 overlap channel 4 and due to the larger count rate in channel 5 the counts in this channel dominate when the fits are made. To quantify the correlation between derived and directly measured electron spectra, we have calculated the energy flux from 3 to 100 keV when comparing with NOAA 12 measurements and from 3 to 30 keV when comparing with DMSP measurements, due to the different energy ranges of the detectors.

**Table 1.** The energy ranges of the channels in the front and rear section of the PIXIE instrument during the two events.

| Section | Front | | | | Rear | |
|---|---|---|---|---|---|---|
| Channels | 20-29 | 30-39 | 40-49 | 50-59 | 10-15 | 16-21 |
| Energy (keV) July 31 | 2.8-4.6 | 4.6-6.3 | 6.3-8.1 | 8.1-9.9 | 7.9-14.6 | 14.6-21.3 |
| Energy (keV) Sept. 4 | 2.7-4.4 | 4.4-6.1 | 6.1-7.7 | 7.7-9.4 | 7.8-14.5 | 14.5-21.2 |

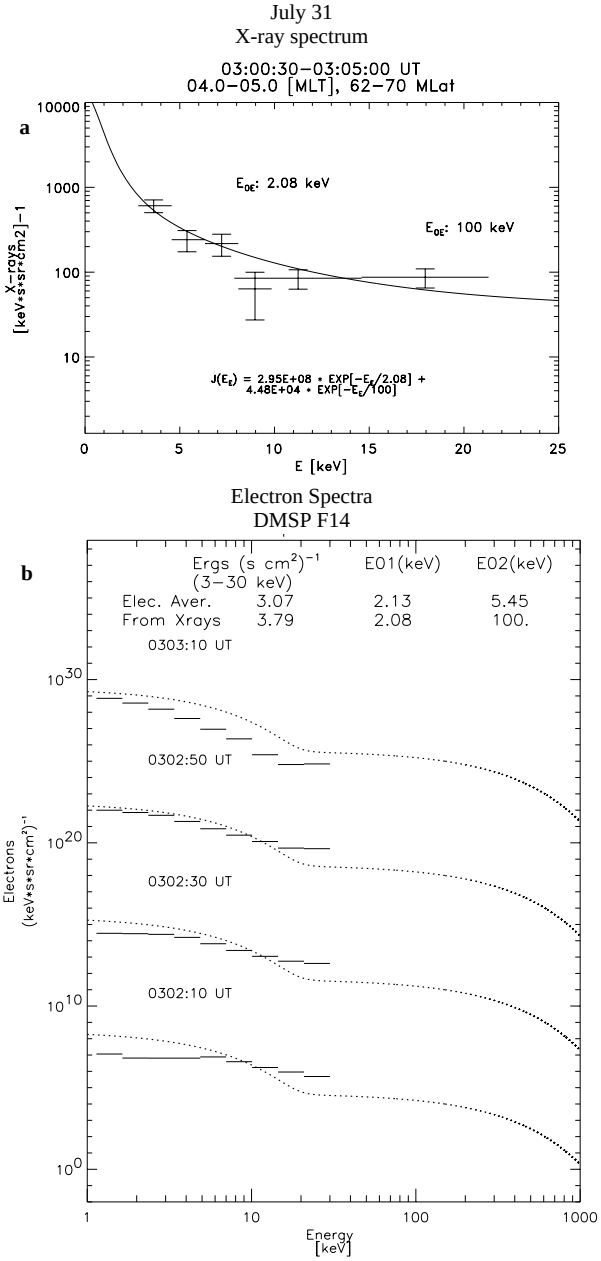


**Figure 7.** (a) Average X-ray spectrum inside the area from 0400-0500 MLT and 62˚-70˚ CGM latitude, July 31, accumulated 0300-0305 UT. The derived double exponential electron spectrum is written on the plot. (b) Horizontal lines show the measured electron spectra by DMSP F14 through the magnetic conjugate area from 0302 to 0303 UT (trajectory for the F14 pass is shown in Figure 4a). Dotted lines show the double exponential electron spectrum derived from the X rays in Figure 7a. The average energy flux (3-30 keV) from the measured spectra and the energy flux from the derived electron spectrum is written on the plot along with values of the e-folding energy values, $E_{01}$ and $E_{02}$, for the two exponentials. The spectra are shifted subsequently by 7 orders of magnitude.

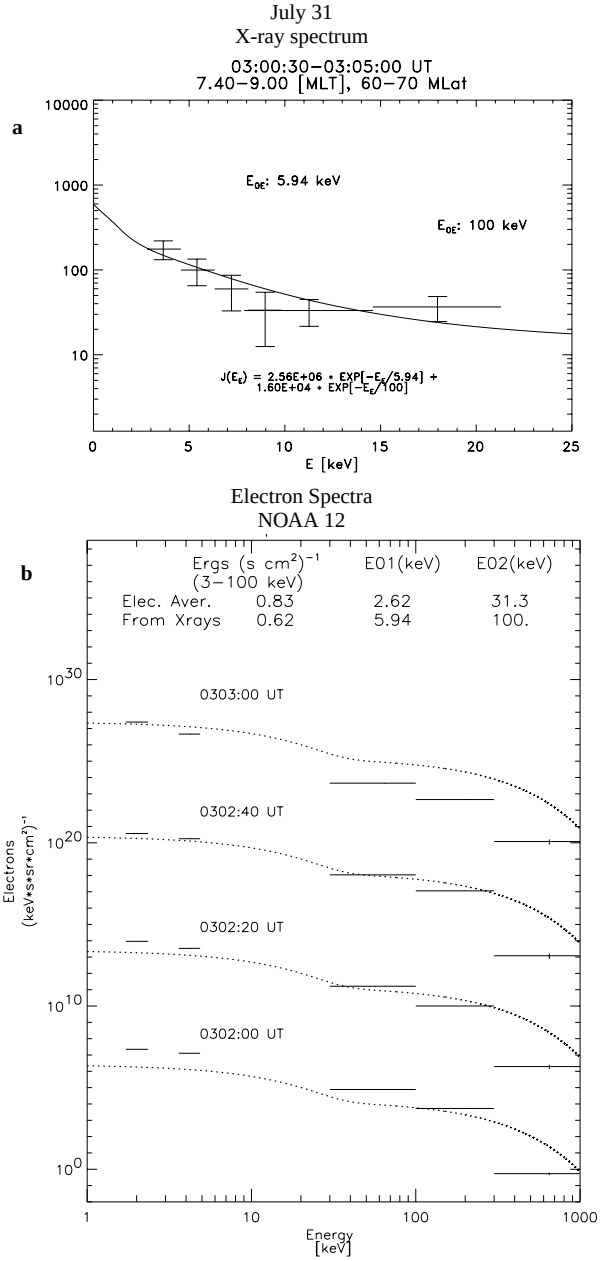


**Figure 8.** (a) Average X-ray spectrum inside the area from 0724-0900 MLT and 60˚-70˚ CGM latitude, July 31, accumulated 0300-0305 UT. The derived double exponential electron spectrum is written on the plot. (b) Horizontal lines show the measured electron spectra by NOAA 12 through the same area from 0302 to 0303 UT (trajectory for the NOAA pass is shown in Figure 4a). Dotted lines show the double exponential electron spectrum derived from the X rays in Figure 8a. The average energy flux (3-100 keV) from the measured spectra and the energy flux from the derived electron spectrum is written on the plot along with values for the two exponentials. The spectra are shifted subsequently by 7 orders of magnitude.

In Figures 7a and 8a we show the X-ray spectra from two different regions in the morning sector accumulated from 0300 to 0305 UT, July 31. The areas are selected to correspond with the satellite passes of DMSP F14 and NOAA 12 (see Figure 4a). The electron measurements correspond very well in time with the X-ray measurements as DMSP F14 passed the 0400-0500 MLT and 62˚-70˚ CGM latitude area from ~0302 to ~0308 UT and NOAA 12 passed the 0724-0900 MLT and 60˚-70˚ CGM latitude area from ~0301 to ~0306 UT. As expected we measure larger X-ray

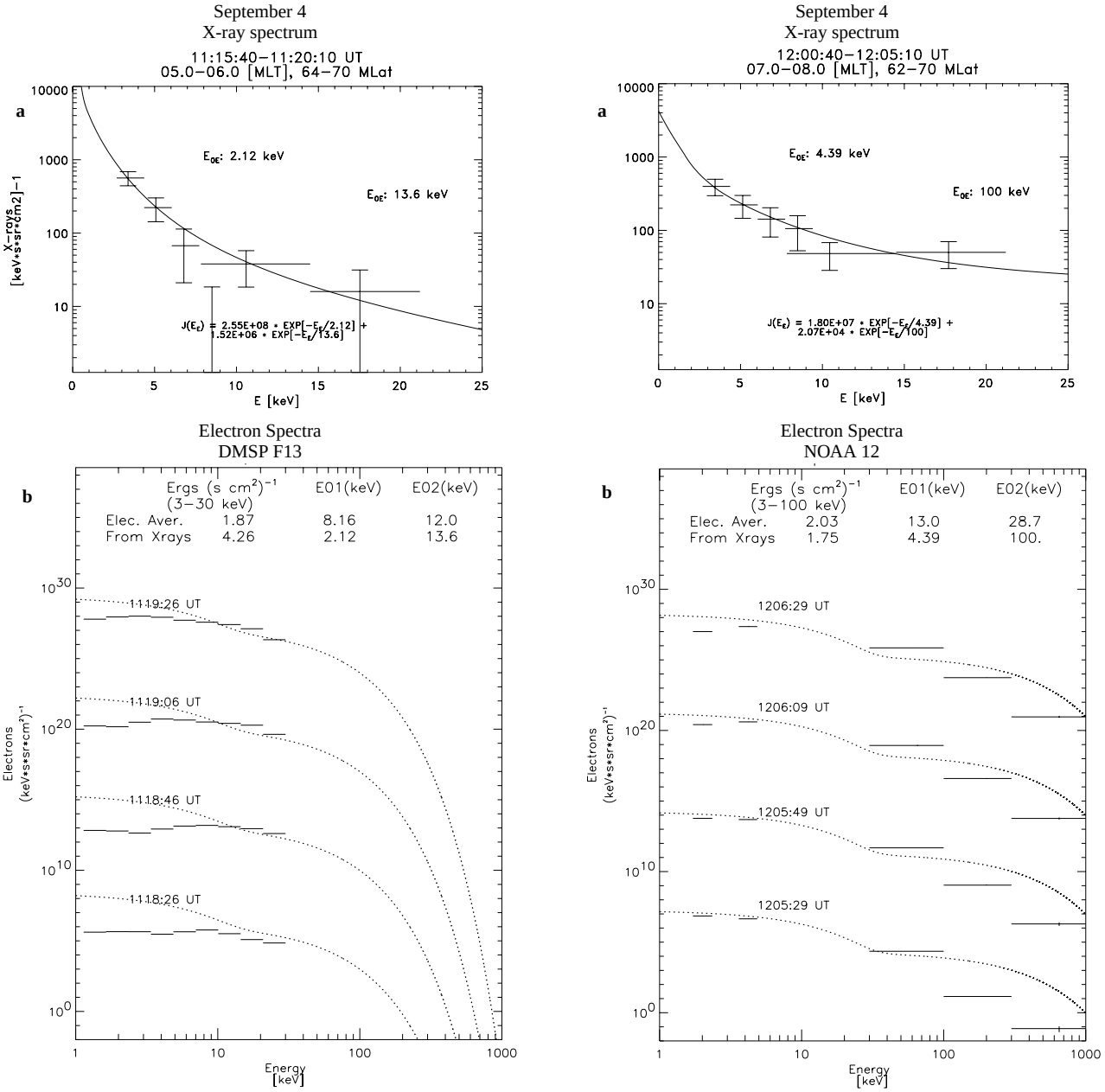


**Figure 9.** (a) Average X-ray spectrum inside the area from 0500-0600 MLT and 64˚-70˚ CGM latitude, September 4, accumulated 1115-1120 UT. The derived double exponential electron spectrum is written on the plot. (b) Horizontal lines show the measured electron spectra by DMSP F13 through the magnetic conjugate area from 1118 to 1119 UT (trajectory for the F13 pass is shown in Figure 5a). Dotted lines show the double exponential electron spectrum derived from the X rays in Figure 9a. The average energy flux (3-30 keV) from the measured spectra and the energy flux from the derived electron spectrum are written on the plot along with values for the two exponentials. The spectra are shifted subsequently by 7 orders of magnitude.

**Figure 10.** (a) Average X-ray spectrum inside the area from 0700-0800 MLT and 62˚-70˚ CGM latitude, September 4, accumulated 1200-1205 UT. The derived double exponential electron spectrum is written on the plot. (b) Horizontal lines show the measured electron spectra by NOAA 12 through the same area from 1205 to 1206 UT (trajectory for the NOAA 12 pass is shown in Figure 6a). Dotted lines show the double exponential electron spectrum derived from the X rays in Figure 10a. The average energy flux (3-100 keV) from the measured spectra and the energy flux from the derived electron spectrum are written on the plot along with values for the two exponentials. The spectra are shifted subsequently by 7 orders of magnitude.

fluxes in the 0400-0500 MLT than in the 0724-0900 MLT sector. The X-ray spectra are rather hard in both regions and consequently the derived electron spectra contains hard tails with e-folding energies of 100 keV. Keeping in mind that the X-ray spectra are based on larger areas, the directly measured electron spectra seem to correlate fairly well with the derived electron spectra from the X-ray measurements. When comparing the energy flux from the derived electron spectra and the directly measured energy flux (i.e., the averages of the four spectra) we have used the energy range of 3-100 keV to be consistent with the energy

range of NOAA 12 measurements, and 3-30 keV when comparing with DMSP. For the two passes we get ~25% larger energy flux for the former and ~25% smaller estimated energy flux for the latter. The low-energy range e-folding values, $E_{01}$, derived from the X-ray spectra are not far from the values from the exponential fit to the measured electron spectra in Figures 7b and 8b. As DMSP does not measure electrons >30 keV, the hard tail derived from the X rays in Figure 7a cannot be extracted from the measured spectra, even if it is slightly seen in the uppermost channels. This also explains why we calculated too low X-ray fluxes from the DMSP measurements in the high-energy range during this pass (Figure 4f).

In Figure 9a we show the X-ray spectrum obtained from September 4, accumulated from 1115 to 1120 UT in 0500-0600 MLT and 64˚-70˚ CGM latitude, i.e., prior to and in the very beginning of the localized maximum of X-ray emission. DMSP F13 passed this region in the Southern Hemisphere at that time. The spectra from F13 at 1118 UT, i.e., just as the maximum appears have a distinct broad peak in the energy range 2-10 keV (see also Plate 2c), which will be discussed in the next section. The high-energy component of the derived electron spectrum correlates well with the high-energy range exponential fit to the directly measured electron spectra. The derived electron energy flux deviates ~130% (Figure 9b).

Our last X-ray spectrum (Figure 10a) is accumulated from 1200 to 1205 UT in 0700-0800 MLT and 62˚-70˚ CGM latitude, i.e., 45 min later during the prolonged morning maximum. The derived electron spectrum is rather hard and correlates fairly well with the NOAA 12 pass (same hemisphere) at the same time. The derived energy flux is in good agreement with the directly measured energy flux. Again, we see an indication of a broad peak in the two upper spectra in Figure 10b spectra at a few keV.

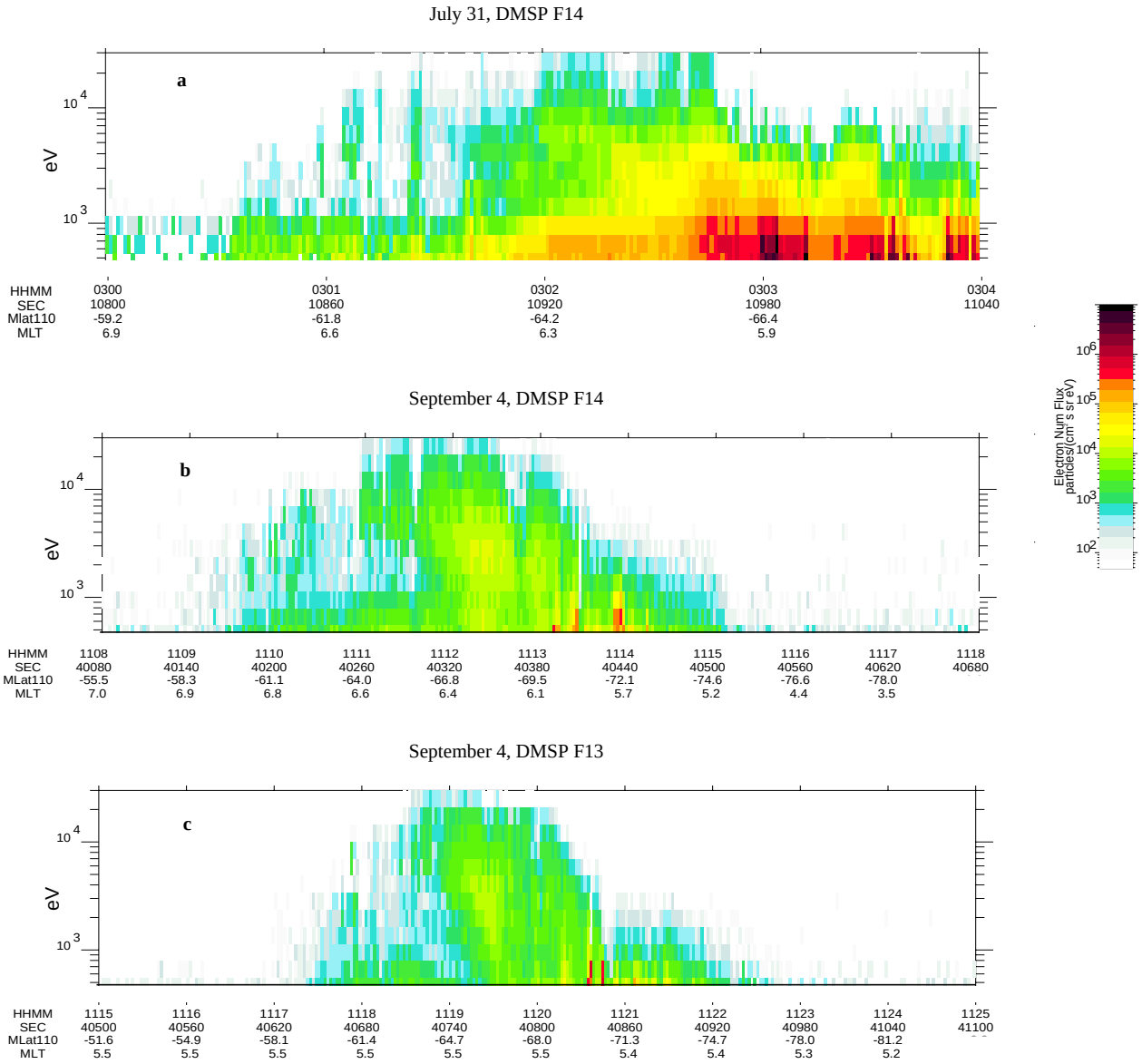


**Plate 2.** Electron spectrograms (0.5-30 keV) from the DMSP satellites during their passes through the region of localized maximum of X-ray emission. The passes are from the Southern Hemisphere in the very beginning the morning maximum: (a) DMSP 14, July 31; (b) DMSP 14, September 4; (c) DMSP 13, September 4.

The global images from PIXIE (Plate 1) and the time analysis of X-ray features along the auroral zone (not shown) have provided the location and temporal extension of the localized maximum of X-ray emission. On the basis of this we know that the DMSP satellite passes in the Southern Hemisphere at ~0302 UT, July 31 (F14) and ~1118 UT, September 4 (F13) are both occurring during the early stage of the morning maximum. The F14 pass at 1111 UT on September 4 occurred 8 min prior to the onset of the localized maximum. The spectrograms from the three passes are shown in Plate 2. For the F14 pass July 31 a peak above ~3 keV can be seen at ~0302 UT at ~64˚ CGM latitude. As the satellite passes the auroral zone at rather slant angle and moves away from the morning maximum region (see Figure 4a), the broad peak is not longer seen. In the spectrograms from F14 and F13 on September 4, which are both from passes crossing only the morning maximum region (Figure 5a) a broad peak in the energy range from 2 to 10 keV is evident at ~64˚-70˚ CGM latitude both prior to (F14 at 1111 UT) and close to onset of the morning maximum (F13 at 1118 UT). We should notice that for both the events the peak is observed at rather low latitudes (~64˚-68˚) and corresponds to the location of the observed X rays (see Figures 4e, 4f and 5).

## 4. Discussion

### 4.1. Validity of the Derived Electron Spectra From the X-ray Measurements

The results regarding the directly measured energy flux and the energy flux derived from the X-ray measurements are summarized in Figure 11. In addition to the four passes shown in Figures 4-10 we have four passes from the DMSP satellites where comparisons have been made, including three passes from July 31 in the midnight 20 min after substorm onset. In Figure 7 it can be seen that for some of the DMSP passes we obtain fairly good agreement for the low-energy e-folding electron energy which is comparable to the lower e-folding energy derived from the X rays, but the frequently observed hard tail in the derived electron spectra is above the threshold of the electron detector and is therefore not measured. For the NOAA 12 passes the e-folding energies in both energy ranges are better correlated. In Figure 11 the squares show the energy flux from NOAA 12 versus PIXIE (both integrated in the energy range 3-100 keV) and crosses show the energy flux from DMSP versus PIXIE (both integrated in the energy range 3-30 keV). Compared to the energy flux derived from X rays, the energy fluxes from the DMSP measurements are systematically underestimated. The energy fluxes measured by NOAA 12 do not show that tendency. The discrepancies might be explained by the lack of pitch angle information from the DMSP measurements and thus we might have included regions of anisotropic electron fluxes which generate more X rays than can be produced by the electrons measured by DMSP. From a similar comparison of PIXIE data and DMSP electron measurements (both at the Southern Hemisphere) by *Anderson et al.* [1998], it can be seen that the derived energy flux and average energy (their Figure 4) from PIXIE correlate very well with the directly measured values from DMSP, but in some region at high latitudes the values obtained from PIXIE exceeds the DMSP values by a factor of ~3, which may be explained by the presence of anisotropic electron fluxes. At this point we may conclude that the derived electron energy spectra from PIXIE seem to give rather good estimates of the energy deposition into the ionosphere. However, when the energy fluxes are derived from electron measurements at small pitch angles, as is the case for the DMSP measurements, they can easily be underestimated.

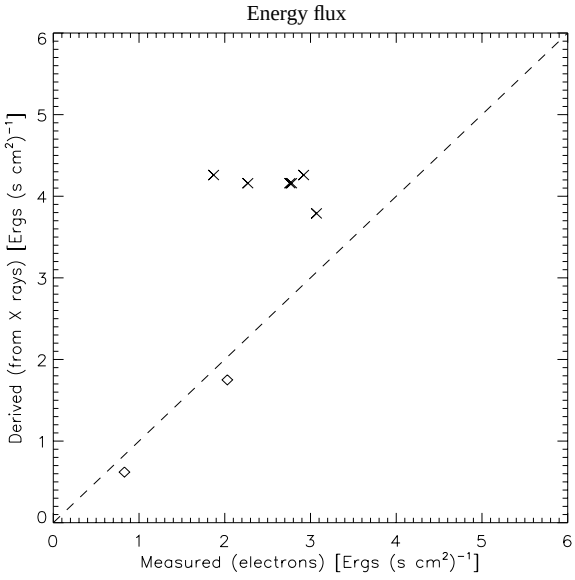


**Figure 11.** Scatterplot of the directly measured electron energy flux and the electron flux from the derived electron spectra from the X-ray measurements. Crosses show DMSP versus PIXIE (3-30 keV) and squares show NOAA 12 versus PIXIE (3-100 keV). The values are taken from Figures 7-10. The ideal regression line is drawn as a dashed line.

### 4.2. Electron Spectral Characteristics of the Localized Maximum of X-ray Emission

In a previous work [*Østgaard et al.*, 1999b] we suggested that either (1) a wave-particle interaction or (2) scattering due to interaction with the magnetopause might be the mechanism that causes the morning maximum of X-ray emission. The spectrograms shown in Plate 2 enable us to examine these hypotheses in more detail. The spectrograms are obtained from passes through the region of localized X-ray emission prior to and during the very beginning of this morning maximum. In all the three panels we can identify a broad peak in the energy range 2-10 keV at rather low latitudes (~64˚-68˚) which corresponds to the location of the observed X rays (see Figures 4e, 4f and 5). In the previous study [*Østgaard et al.*, 1999b] we reported that the localized morning maximum was rarely seen in the UV images, indicating rather high precipitating electron energies. However, for the July 31 event we see the morning maximum in the UVI as well, which is consistent with the electron peak in the energy range 2-10 keV observed by DMSP. For the September 4 event the FOV of UVI was not covering the morning sector. The observations of this broad peak at ~2-10 keV in the DMSP data during these two events exclude some of the proposed mechanism for the morning maximum.

1. The morning maximum observed during these two event cannot be explained by the scattering of electrons at the magnetopause, as the X-ray emission (as well as the broad peak in the spectrograms) is observed well below 70˚ CGM latitude and consequently the field lines are probably well within the magnetopause.

2. The broadness of the peak indicates no monoenergetic beam, a signature which is usually related to arcs and inverted V events in the premidnight sector caused by parallel electric fields and unlikely to be observed at the dawnside.

3. The broad peak is observed too early to be caused by a mechanism triggered by the drifting electrons from the injected particles in the substorm onset region near midnight. For the September 4 event the broad peak is present both at passes prior to and after (i.e., ±101 min, spectrograms not shown) the onset of the localized morning maximum but varies in intensity. This does not prevent the arrival of drifting electrons to increase the effect of the mechanism.

However, the broad peak may be consistently interpreted as caused by a wave-particle interaction which is more or less continuously present in the morning region and that the strength of the process depends on the anisotropic fluxes of electrons. The shape of the observed spectra in our study (Figures 7 and 9, and Plate 2) indicates that the wave-particle interaction acts on electrons down to a few keV. Then we arrive at a similar conclusion as *Jelly and Brice* [1967] did, as they suggested that the anisotropy of unstably quasi-trapped electrons is largely determined by the loss cone and hence the instability is determined solely on the flux level, i.e., if the flux exceeds the threshold for the instability to work. This threshold is known as the maximum stable limit for fluxes of trapped energetic electrons suggested by *Kennel and Petscek* [1966]. However, *Jentsch* [1976] has shown that an anisotropy is established without introducing the loss cone and the conclusion may therefore be modified at this point, as will be discussed below. When the electron cloud injected at substorm onset enters this region the wave-particle interaction increases and will go on as long as there are sufficient fluxes of anisotropic trapped electrons. From Figure 1a we saw that the September 4 event occurred in the recovery phase of a magnetic storm, and it is therefore likely that there existed sufficient trapped electron fluxes from previous magnetic activity for the wave-particle interaction to work. The July 31 event took place after a long quiet period (Figure 1b), and the number of trapped electrons was probably lower. This may explain why the broad peak is more pronounced in the September 4 event than the July 31 event.

For parallel propagating waves the Doppler-shifted electron cyclotron wave-particle interaction involving VLF frequencies will act upon electrons with energies $>E_{c\parallel} = {}^1/_2\, m v_\parallel^2$, where $v_\parallel$ is the resonant parallel velocity component. The resonance condition for parallel propagating waves, linear approximation is given by (2) and, when all terms are used, by (3).

$$E_{c\parallel} = \frac{B^2}{8\pi n}\frac{\Omega}{\omega} \tag{2}$$

$$E_{c\parallel} = \frac{B^2}{8\pi n}\frac{\Omega}{\omega}\left(1-\frac{\omega}{\Omega}\right)^3, \tag{3}$$

where $B$ is the magnetic field strength, $n$ is the electron density, $\omega$ is the wave frequency and $\Omega$ is the electron gyro frequency. $\omega$ is usually found to be ~1/2 $\Omega$, which lower the parallel resonant energy by a factor of 8 compared to the linear approximation often used (2). Modelling of wave growth-rates based on *Kennel and Petscek* [1966], which can account for the observed features have been performed by *Jentsch* [1976] using $n$=10 cm$^{-3}$ and electron energies >40 keV. The lower threshold of electron energy was partly chosen to avoid the effect of the convective electric field on the electron drift trajectories and his results do not exclude lower electron energies to be involved in the wave-particle interaction. As he used an isotropic electron distribution to model the injected electrons, and no loss mechanism were introduced, the anisotropic electron fluxes solely resulted from the different drift velocities for electrons at different pitch angles in the magnetic and the electric field, i.e., no loss cone was needed to obtain the anisotropic fluxes. He performed his calculations of wave growth rates for three different magnetic field models and it should be noticed that the most realistic magnetic field model, i.e., a model by *Mead* [1964] resulted in a maximum anisotropy and a maximum wave growth around 0500-0900 MLT, while introducing a convective electric field tended to shift the maximum anisotropy towards noon. The introduction of an inhomogenous magnetic field is essential in order to establish the anisotropy needed and to explain why a maximum of wave-particle interaction is observed just in the morning sector. At this point we think *Jentsch* [1976] provides a valuable modification to the theory suggested by *Jelly and Brice* [1967]. In a survey study of ELF/VLF waves at geosynchronous orbit, *Parrot and Gaye* [1994] reported that chorus of 400-700 Hz show a distinct peak between 0600-0900 MLT. Simultaneous measurements of VLF waves and the angular distribution of electron fluxes in the morning sector are scarce, but a study of *Isenberg et al.* [1982] based on measurements from the P78-2 (SCATHA) satellite reports some interesting results for the purpose of this study. Examining angular electron distribution in the energy range from 12 to 81.5 keV and VLF frequencies from 0.4 to 3.0 kHz, they found that the dawnside chorus between 5.3 $<L<$7.8 is generated by substorm-injected, anisotropic fluxes of electrons with energies between 10 and 100 keV. Taking into account what pitch angles of electrons that are responsible for the wave growth (i.e., $\alpha$=40˚-50˚), the observed waves can very well be interacting with electrons down to ~1-20 keV in the vicinity of the loss cone. It should also be noticed that >3 kHz wave measurements were not available and consequently they have no measurements that could have been correlated with the anisotropic electron fluxes at even lower electron energies. In their data, anisotropic fluxes is clearly seen down to 12.1 keV, which is the lowest channel they show. Depending on the pitch angle distribution, this may well be consistent with waves acting on electrons down to a few keV in the vicinity of the loss cone. We may conclude that the study of *Isenberg et al.* [1982] partly support our interpretation of the broad peak in the electron distribution observed by DMSP to be caused by the scattering due to wave-particle interaction.

## 5. Conclusion

In this study we have examined global X-ray images and electron measurements from low-altitude satellites in order to obtain information about the localized maximum of X-ray emission in the morning sector. In doing this we have also developed a method to derive electron spectra from X-ray spectra. To summarize, we have found the following:

1. The two isolated substorms of July 31 and September 4 show the same global characteristics as found by *Østgaard et al.* [1999b]. The localized maximum of X-ray emission in the morning sector delayed relative to the substorm onset is observed in both the events.

2. In order to calculate the X-ray production from electron spectra we have found that the sum of two exponentials may represent the electron spectra fairly well both in the midnight and the morning sector. In the very high-energy range of the electron measurements a Kappa function would probably have made a bet-

ter fit, but the uncertainties introduced by using the exponentials are probably very small as the fluxes at these energies are very low.

3. Through the region of localized maximum we find good spatial and quantitative correlation between observed X rays and the X-ray production estimated from the directly measured electron distribution. In the region of isotropic electron fluxes the correspondence is often close to the statistical errors of the X-ray measurements and the discrepancies observed outside this region are most probably due to anisotropic electron fluxes at pitch angles outside the detectors FOV but well within the atmospheric loss cone.

4. By fitting the X-ray spectra by double or single exponentials we have developed a method of deriving electron spectra and the energy deposition into the ionosphere which corresponds within a factor of two to the directly measured energy fluxes. When the pitch angle distribution within the loss cone is not known, energy fluxes derived from insitu electron measurements can very well be underestimated. Thus the energy flux derived from the X rays probably gives a better estimate of the energy flux deposited in the ionosphere.

5. The electron energy spectra observed prior to, at the initial stage of, and after the localized morning maximum of X-ray strongly indicates that a wave-particle interaction is the main mechanism for the enhancements observed.

6. VLF waves are probably excited more or less continuously by quasi-trapped anisotropic fluxes of electrons from tens of keV up to hundreds of keV and the wave growth are further raised by the arrival of the injected anisotropic fluxes injected at midnight drifted into the morning sector. As *Jentsch* [1976] has shown, the anisotropy of unstably quasi-trapped electrons will result from the different drift velocities of electrons at different pitch angles and is significantly affected by the magnetic field configuration and the presence of any increased electric field. He has shown that the stretched magnetic field configuration can account for a maximum of anisotropy and wave growth in the 0500-0900 MLT sector. The loss cone will lead to an even stronger anisotropy. The instability and the strength of wave-particle interaction is therefore determined mainly by the flux level [*Jelly and Brice*, 1967], but the location of the maximum is determined by the magnetic field configuration [*Jentsch*, 1976]. If the fluxes of electrons exceed the maximum stable limit for fluxes of trapped energetic electrons energy are transferred from the electrons to the waves and the wave growth will act back on the electrons and effectively scatter them into the loss cone [*Kennel and Petscek*, 1966, *Jelly and Brice*, 1967]. For the two events in this study the waves seem to act on electrons down to a few keV. As long as there is sufficient fluxes of trapped anisotropic electrons, the process will go on and thus can account for the prolonged maximum observed.

7. Previous simultaneous measurements of anisotropic electron fluxes and VLF waves give some support for the presence of VLF waves which are able to act upon electrons of energies down to just a few keV.

**Acknowledgments.** This study was supported by the Norwegian Research Council (NFR) and by the National Aeronautics and Space Administration under contract NAS5-30372 at the Lockheed-Martin Advanced Technology Center. We want to thank D. Evans at SEL/NOAA for providing particle measurements from the NOAA 12 satellite and F. Rich at Space Physics Model Branch for providing data from the SSJ/4 particle detectors on board the DMSP satellites. We are also grateful to the World Data Center - C2 (T. Kamei) in Kyoto, Japan, for making preliminary quick look *AE* indices available via Internet.

Janet G. Luhmann thanks Per Even Sandholt and another referee for their assistance in evaluating this paper.

## References

Anderson, P. C., D. L. Chenette, D. L. McKenzie, J. M. Quinn, M. Grande, and M. Carter, Energetic auroral electron distribution derived from global x-ray measurements and comparison with in-situ particle measurements, *Geophys. Res. Lett.*, *25*, 4105–4108, 1998.

Barcus, J. R., and T. J. Rosenberg, Energy spectrum for auroral-zone X rays, 1, Diurnal and type effects, *J. Geophys. Res.*, *71*, 803–823, 1966.

Berger, M. J., and S. M. Seltzer, Bremsstrahlung in the atmosphere, *J. Atmos. Terr. Phys.*, *34*, 85–108, 1972.

Berkey, F. T., V. M. Driatskij, K. Henriksen, B. Hultqvist, D. Jelly, T. I. Shchuka, A. Theander, and J. Yliniemi, A synoptic investigation of particle precipitation dynamics for 60 substorms in IQSY(1964-65) and IASY(1969), *Planet. Space Sci.*, *22*, 255–307, 1974.

Bjordal, J., H. Trefall, S. Ullaland, A. Bewersdorff, J. Kangas, P. Tanskanen, G. Kremser, K. H. Saeger, and H. Specht, On the morphology of auroral-zone X-ray events, I, Dynamics of midnight events, *J. Atmos. Terr. Phys.*, *33*, 605–626, 1971.

Chenette, D. C., D. W. Datlowe, W. L. Imhof, T. L. Schumaker, and J. D. Tobin, Global spectroscopy and imaging of atmospheric X-ray bremsstrahlung: Instrumentation and initial results from the PEM/AXIS instrument aboard the Upper Atmosphere Research Satellite, *Proc. SPIE Int. Soc. Opt. Eng.*, *1745*, 16–25, 1992.

Codrescu, M. V., T. J. Fuller-Rowell, R. Roble, and D. S. Evans, Medium energy particle precipitation influence on the mesosphere and lower thermosphere, *J. Geophys. Res.*, *102*, 19,977–19,987, 1997.

Goldberg, R. A., J. R. Barcus, L. A. Treinish, and R. R. Vondrak, Mapping of auroral X rays from rocket overflights, *J. Geophys. Res.*, *87*, 2509–2524, 1982.

Hardy, D. A., L. K. Schmitt, M. S. Gussenhoven, F. J. Marshall, H. C. Yeh, T. L. Shumaker, A. Hube, and J. Pantazis, Precipitating electron and ion detectors (SSJ/4) for the block 5D/flights 6-10 DMSP satellites: Calibartion and data presentation. *Rep. AFGL-TR-84-0317*, Air Force Geophys. Lab., Hanscom Air Force Base, Mass., 1984.

Hardy, D. A., M. S. Gussenhoven, and E. Holeman, A statistical model of auroral electron precipitation, *J. Geophys. Res.*, *90*, 4229–4248, 1985.

Hartz, T. H., and N. M. Brice, The general pattern of auroral particle precipitation, *Planet. Space Sci.*, *15*, 301–329, 1967.

Imhof, W. L., J. R. Kilner, G. H. Nakano, and J. B. Reagan, Satellite X-ray mappings of sporadic auroral zone electron precipitation events in the local dusk sector, *J. Geophys. Res.*, *85*, 3347–3359, 1980.

Imhof, W. L., et al., The Polar Ionospheric X-ray Imaging Experiment (PIXIE), *Space Sci. Rev.*, *71*, 385–408, 1995.

Isenberg, P. A., H. C. Koons, and J. F. Fennell, Simultaneous observations of energetic electrons and dawnside chorus in geosynchronous orbit, *J. Geophys. Res.*, *87*, 1495–1503, 1982.

Jelly, D., and N. Brice, Changes in Van Allen radiation associated with polar substorms, *J. Geophys. Res.*, *72*, 5919–5931, 1967.

Jentsch, V., Electron precipitation in the morning sector of the auroral zone, *J. Geophys. Res.*, *81*, 135–146, 1976.

Kangas, J., L. Lukkari, P. Tanskanen, H. Trefall, J. Stadsnes, G. Kremser, and W. Riedler, On the morphology of auroral-zone X-ray events, IV, Substorm-related electron precipitation in the local morning sector, *J. Atmos. Terr. Phys.*, *37*, 1289–1303, 1975.

Kennel, C. F., and H. E. Petscek, Limit on stably trapped particle fluxes, *J. Geophys. Res.*, *71*, 1–28, 1966.

Lew, J. A., Drift rate in a dipole field, *J. Geophys. Res.*, *66*, 2681–2685, 1961.

Liou, K., P. T. Newell, and C. I. Meng, Synoptic auroral distribution: A survey using Polar ultraviolet imagery, *J. Geophys. Res.*, *102*, 27,197–27,205, 1997.

Lorence, L. J., CEPXS/ONELD Version 2.0: A discrete ordinates code package for general one-dimensional coupled electron-photon transport, *IEEE Trans. Nucl. Sci.*, *39*, 1031–1034, 1992.

McDiarmid, I. B., J. R. Burrows, and E. E. Budzinski, Average characteristics of magnetospheric electrons (140 eV to 200 keV) at 1400 kilometers, *J. Geophys. Res.*, *80*, 73–79, 1975.

Mead, G. D., Deformation of the geomagnetic field by the solar wind, *J. Geophys. Res.*, *69*, 1181–1195, 1964.

Østgaard, N., J. Stadsnes, K. Aarsnes, F. Søraas, K. Måseide, M. Smith, and J. Sharber, Simultaneous measurements of X rays and electrons during a pulsating aurora, *Ann. Geophys.*, *16*, 148–160, 1998.

Østgaard, N., J. Stadsnes, J. Bjordal, R. R. Vondrak, S. A. Cummer, D. C. M. Schulz, G. K. Parks, M. J. Brittnacher, D. L. McKenzie, and J. G. Pronko, Global X-ray emission during an isolated substorm - A case study, *J. Atmos. Terr. Phys.*, in press, 1999a.

Østgaard, N., J. Stadsnes, J. Bjordal, R. R. Vondrak, S. A. Cummer, D. Chenette, G. K. Parks, M. J. Brittnacher, and D. L. McKenzie, Global scale electron precipitation features seen in UV and X rays during substorms, *J. Geophys. Res.*, *104*, 10,191–10,204, 1999b.

Parrot, M., and C. A. Gaye, A statistical survey of ELF waves in a geostationary orbit, *Geophys. Res. Lett.*, *21*, 2463–2466, 1994.

Petrinec, S. M., J. Mobilia, D. Chenette, W. L. Imhof, and F. Fenrich, Statistical survey of auroral X-ray emissions: PIXIE observations, in *Proceedings of the International Conference on Substorms*, vol. 4, edited by Y. Kamide, pp. 809–812, Terra Sci., Tokyo, 1998.

Raben, V. J., D. S. Evans, H. H. Sauer, S. R. Sahm, and M. Huynh, TIROS/NOAA satellite environment monitor data archive documentation: 1995 update, technical report, Space Environ. Lab., Boulder, Colo., 1995.

Roederer, J. G., *Dynamics of Geomagnetically Trapped Radiation*, Springer Verlag, New York, 1970.

Sharber, J. R., R. A. Frahm, R. Link, G. Crowley, J. D. Winningham, E. E. Gaines, R. W. Nightingale, D. L. Chenette, B. J. Anderson, and C. A. Gurgiolo, UARS Particle Enviroment Monitor observations during the november 1993 storm: Auroral morphology, spectral characterization, and energy deposition, *J. Geophys. Res.*, *103*, 26,307–26,322, 1998.

Sletten, A., J. Stadsnes, and H. Trefall, Auroral-zone X-ray events and their relation to polar magnetic substorms, *J. Atmos. Terr. Phys.*, *33*, 589–604, 1971.

N. Østgaard, Department of Physics, University of Oslo, N-0316 Oslo, Norway. (Nikolai.Ostgaard@fys.uio.no)

J. Bjordal and J. Stadsnes, Department of Physics, University of Bergen, N-5007 Bergen, Norway.

D. L. Chenette and M. Shulz, Lockheed Martin Advanced Technology Center, Palo Alto, CA 94304.

S. A Cummer, Department of Electrical and Computer Engineering, Duke University, Durham, NC 27708

R. R. Vondrak, Laboratory for Extraterrestrial Physics, Goddard Space Flight Center, Greenbelt, MD 20771.

J. G. Pronko, Physics Department, University of Nevada, Reno, NV 89507

(Received September 24, 1999; November 9, 1999;
accepted November 9, 1999)

[1]Department of Physics, University of Bergen, Bergen, Norway.
[2]Now at Department of Physics, University of Oslo, Oslo, Norway.
[3]Laboratory for Extraterrestrial Physics, Goddard Space Flight Center, Greenbelt, Maryland.
[4]Now at Department of Electrical and Computer Engineering, Duke University, Durham, North Carolina.
[5]Lockheed Martin Advanced Technology Center, Palo Alto, California.
[6]Physics Department, University of Nevada, Reno.

Copyright 2000 by the American Geophysical Union

Paper number 1999JA000354.
0148-0227/00/1999JA000354$09.00